

# Origin of the scatter in the X-ray luminosity of early-type galaxies observed with ROSAT

KYOKO MATSUSHITA<sup>1</sup>

Received \_\_\_\_\_; accepted \_\_\_\_\_

---

<sup>1</sup>Max-Planck-Institut für extraterrestrische physik, D-85740, Garching, Germany;  
matusita@xray.mpe.mpg.de

## ABSTRACT

Statistical properties of X-ray luminosity and temperature are studied for 52 early-type galaxies based on the ROSAT PSPC data. All of the X-ray luminous galaxies show largely extended emission with a radius of a few times of  $10r_e$ , while X-ray faint galaxies do not show such a component. This leads to a division of early-type galaxies into two categories: X-ray extended and X-ray compact galaxies. Except for a few galaxies in dense cluster environments, the luminosity and temperature of X-ray compact galaxies are well explained by a kinematical heating of the gas supplied by stellar mass loss. In contrast, X-ray extended galaxies indicate large scatter in the X-ray luminosity. We discuss that X-ray extended galaxies are the central objects of large potential structures, and the presence and absence of this potential is the main origin of the large scatter in the X-ray luminosity.

*Subject headings:* X-rays:galaxies — galaxies:ISM — ISM:luminosity

## 1. Introduction

Giant early-type galaxies are luminous X-ray emitters (e.g. Forman et al. 1985, Trinchieri et al. 1986). Studies from the *Einstein* observatory showed the origin of X-rays to be hot interstellar medium (ISM) with a temperature of  $\sim 1$  keV and discrete sources such as low-mass X-ray binaries (LMXBs). The hot ISM is considered to be gravitationally confined in a galaxy, X-ray observations provide an efficient method to look into the shape of the gravitational potential which traces the dark matter distribution.

An additional very soft component (VSC) is often seen in the X-ray spectra of very faint early-type galaxies, characterized by a temperature of 0.1–0.3 keV (Kim et al. 1992; Fabbiano et al. 1994; Pellegrini et al. 1994; Irwin and Sarazin 1998a). The nature of VSC is not clear yet.

X-ray luminosities ( $L_X$ ) of early-type galaxies vary by two orders of magnitude for the same optical B-band luminosity ( $L_B$ ) (Trinchieri et al. 1985, Canizares et al. 1987, Fabbiano et al. 1992). Beuing et al. (1999) confirmed the same  $L_X$  scatter based on the ROSAT all-sky survey. On the other hand, the existence of the fundamental plane indicates that elliptical galaxies are dynamically uniform systems (e.g Djorgovski, & Davis 1987; Bender et al. 1993). It is, therefore, quite difficult to understand why X-ray luminosity of ISM scatters so largely.

Various explanations for the origin of this  $L_X$  scatter have been proposed. Eskridge et al. (1995) discovered a strong correlation between  $L_X/L_B$  and potential depth, or stellar velocity dispersion. White and Sarazin (1991) found that galaxies in a high local galaxy density tend to be X-ray faint. They conclude that the interaction with other galaxies or surrounding ICM (intra-cluster medium) strips the ISM from the galaxies.

Extended X-ray emission has been detected from several X-ray luminous early-type

galaxies (Trinchieri et al. 1994; Trinchieri et al. 1997). Mathews et al. (1998) showed that X-ray luminous galaxies maintain larger emission region than X-ray faint galaxies. With ASCA, Matsushita et al. (1998) discovered a greatly extended X-ray emission up to 300 kpc around NGC 4636. The gravitational mass profile of NGC 4636 indicate that the galaxy lies in the bottom of a group-scale potential structure filled with a tenuous hot plasma. Such extended X-ray emission has been detected in other X-ray luminous galaxies with ASCA (Matsushita 1997). We suggest that the presence or absence of such a greatly extended X-ray emission is the main origin for the scatter of the X-ray luminosity (Matsushita et al. 1998).

To address this issue, we need information for a larger sample of objects. Correct estimation for the X-ray luminosity of hot ISM has to be made by removing the contribution from discrete sources. After this, we can investigate the systematic difference between X-ray luminous and X-ray faint galaxies regarding the shape of the ISM distribution. This paper reports statistical X-ray properties of early-type galaxies, such as luminosity, spatial distributions of brightness and temperature, based on the ROSAT data, which offer a much larger sample than those of ASCA.

Galaxy distances are derived assuming the Hubble constant of  $H_0 = 75 \text{ km s}^{-1} \text{ Mpc}^{-1}$ , using Faber et al. (1989) group distance. We adopt the ‘meteoritic’ solar iron abundance,  $\text{Fe/H} = 3.24 \times 10^{-5}$  in number, given by Anders & Grevesse (1989).

## 2. Targets and Observations

The early-type galaxies selected from the ROSAT PSPC archival data have total B-band magnitude ( $m_B$ ) larger than 11.71 and B-band luminosity ( $L_B$ ) larger than  $10^9 L_\odot$ . The sample consists of 52 galaxies as listed in table 1. It includes  $\sim 80\%$  of elliptical and

~ 20% of S0 galaxies which satisfy the selection criterion, in the Nearby Galaxy Catalog by Tully (1998). Nineteen galaxies are located in clusters, including 3 cD galaxies in the Virgo, Fornax and Centaurus clusters: which are NGC 1399, NGC 4486, and NGC 4696. The remaining 33 galaxies are either in the field or in small groups. The galaxies in the above 3 clusters are called cluster galaxies, and others are called field galaxies, hereafter.

### 3. Analysis and Results

#### 3.1. Integration region and background

The PSPC data were accumulated in 3 annular regions,  $0\text{--}4r_e$ ,  $4\text{--}12r_e$ , and  $12\text{--}30r_e$ , centered on each galaxy. Here  $r_e$  is the effective radius of each galaxy (from the RC3 Catalog). Background is taken in a nearby outer region for each data set. An annular region with  $12\text{--}14r_e$  and  $30\text{--}40r_e$  is chosen for the data in  $0\text{--}12r_e$  and  $12\text{--}30r_e$ , respectively. This procedure gives an automatic correction for an extended emission component such as an ICM contribution. We also exclude regions within  $1'$  from discrete point sources when their signal-to-noise ratios are greater than 4.

The PSPC spectra within  $4r_e$  are fitted with a standard two hard component model: the Raymond & Smith (1977) thin thermal emission for the ISM, and thermal bremsstrahlung with a fixed temperature at 10 keV which models the contribution from LMXBs (Matsushita et al. 1994). The two components are allowed to have free normalization, but are subjected to a common absorption by a free column density,  $N_{\text{H}}$ . For faint galaxies, with the ISM flux in  $4\text{--}12r_e$  or in  $12\text{--}30r_e$  less than  $3 \times 10^{-13} \text{ erg cm}^{-2} \text{s}^{-1}$ , we fixed the ISM temperature at the best-fit value obtained within  $4r_e$ . Abundances of heavy elements are organized into two groups:  $\alpha$ -elements (O, Ne, Mg, Si and S) and Fe group (Fe and Ni). Since PSPC data are not very sensitive to metal abundance, the  $\alpha$ -element

abundance in the thermal component is assumed to be 1 solar following the extensive study by Matsushita et al. (2000). For every spectrum, when the ISM component flux is lower than  $1.5 \times 10^{-12}$  erg cm $^{-2}$ s $^{-1}$ , Fe abundance is fixed to 0.5 solar.

Figure 1 shows the PSPC spectra for several representative galaxies with different X-ray luminosities, fitted with the two component model. The soft ISM emission and the hard bremsstrahlung component are distinguishable, and a single temperature model obviously gives wrong values of ISM luminosity and temperature. The discrepancy would be larger for X-ray faint galaxies, whose emission is more dominated by LMXBs. Thus, the two component model is necessary in separating the pure ISM component.

We summarize the spectral results in table 2. Most of the galaxies indicate an absorption which is consistent with the Galactic level, within  $10^{20}$  cm $^{-2}$ .

### 3.2. The ISM luminosity

#### 3.2.1. X-ray extended and X-ray compact galaxies

Figure 2 shows the derived the ISM luminosities in the energy band 0.2-2.0 keV for 3 annular regions: within  $4 r_e (L_X(<4r_e))$ ,  $4\text{--}12 r_e (L_X(4\text{--}12r_e))$ , and  $12\text{--}30 r_e (L_X(12\text{--}30r_e))$ . The derived luminosity values are absorption-corrected. Significant X-ray emission from ISM is detected for 43 galaxies, and the remaining 9 galaxies give upper limits. The measured range of  $L_X(<4r_e)$  is from  $10^{39}$  erg s $^{-1}$  to  $10^{43}$  erg s $^{-1}$ . The ISM emission in the outer  $4\text{--}12r_e$  and  $12\text{--}30r_e$  regions is detected for only 15 and 9 galaxies, respectively.

For X-ray luminous galaxies, the ISM luminosity values are mostly consistent with the published results with some difference due to the selection of accumulating region (Trinchieri et al. 1985, Canizares et al. 1987, Fabbiano et al. 1992, Irwin & Sarazin 1998b, Beuing et al. 1999). Our results for X-ray fainter galaxies are significantly smaller than

the earlier ones, since previous values mostly include contribution from the hard spectral component. Also, the central luminosities,  $L_X(<4r_e)$ , are consistent with the ASCA results (Matsushita et al. 2000), when the difference in the energy range is corrected.

X-ray luminous ( $L_X(<4r_e) > 10^{41} \text{ erg s}^{-1}$ ) galaxies show comparable levels of  $L_X(4-12r_e)$  and  $L_X(12-30r_e)$ , and they correlate well with the central  $L_X(<4r_e)$ . This correlation is less clear for X-ray fainter galaxies mainly because of the large uncertainty.

The spatial extent of the X-ray emission is parametrized using a ratio of the annular luminosities. The ratios  $L_X(4-12r_e)/L_X(<4r_e)$  and  $L_X(12-30r_e)/L_X(<4r_e)$  are denoted as S4–12 and S12–30, respectively, and larger values indicate more extended emission. Figure 3 shows S4–12 and S12–30 values against  $L_X(<4r_e)$ . All of the X-ray luminous ( $L_X(<4r_e) > 10^{41} \text{ erg s}^{-1}$ ) galaxies have S4–12 and S12–30 to be 0.3–1.3 and 0.5–2, respectively. If the ISM brightness profile follows the optical  $r^{1/4}$  law, these values should be 0.13 and 0.03, respectively. Thus, X-ray luminous galaxies clearly show much more extended emissions than the optical profile.

In contrast, all of the S12–30 of galaxies with  $L_X(<4r_e) < 10^{40.0-40.8} \text{ erg s}^{-1}$  are less than  $\sim 0.5$ , although 3 galaxies, NGC 1395, NGC 3607, and NGC 4382, have comparable level of S4–12 as in the X-ray luminous galaxies. Therefore, the X-ray fainter galaxies tend to have more compact emission.

Hereafter, we denote these X-ray extended galaxies, whose S12–30 are larger than 0.4, as “X-ray extended” galaxies and others as “X-ray compact” galaxies. The objects classified as X-ray extended galaxies are NGC 1399 (cD of Fornax), NGC 1407 (Group center), NGC 4406 (Virgo), NGC 4472 (Virgo), NGC 4486 (cD of Virgo), NGC 4636 (Virgo), NGC 4696 (cD of Cen), NGC 5044 (Group center), and NGC 5846 (Group center). All of these galaxies are elliptical galaxies

### 3.2.2. The scatter of X-ray luminosities against optical properties

The relation of  $L_X(<4r_e)$  to optical B-band luminosity ( $L_B$ ) is shown in Figure 4. The scatter of the ISM luminosities within the given optical radii is two orders of magnitude for the same optical luminosity. It is clear that the X-ray extended galaxies show larger  $L_X/L_B$  values than the X-ray compact ones, and the division into these two categories significantly reduces the  $L_X$  scatter particularly for the X-ray compact galaxies.

For quantitative evaluation, we fit the distributions in Figure 4. We employ the same method in fitting the X-ray luminosity distribution as the one for the Einstein data analysis (Fabbiano & Trinchieri 1985, Trinchieri & Fabbiano 1985, Canizares et al. 1987). The distribution function is assumed to be Gaussian with a fixed standard deviation  $s$  around a straight line;  $\log L_X = a(\log L_B - 11.0) + b$ , where  $a$ ,  $b$  and  $s$  are free parameters. We use the maximum-likelihood method developed by Anvi (1980), in which both detections and upper limits are assumed to come from the same parent population.

The fitting results are summarized in Table 3. The whole sample gives the standard deviation  $s$  to be 0.7, which is larger than 0.48 derived from the Einstein sample (Canizares et al. 1997). This is because we have separated the pure ISM component from the rather constant discrete-source contribution. The best-fit slope is 1.9, which is similar to 1.7 and 2.2 derived from the Einstein (Canizares et al. 1987) and ROSAT (Beuing et al. 1999) data, respectively.

The deviation  $s$  is reduced to 0.40 and 0.45 for the X-ray extended and the X-ray compact galaxies, respectively. This indicates that the large scatter of the X-ray luminosity is mainly caused by existence of the largely extended X-ray emission. For the X-ray compact galaxies, the slope parameter also drops to 1.5.

Figure 4 also shows correlation between  $L_X(<4r_e)$  against  $L_B\sigma^2$ , with  $\sigma^2$  denoting a

central stellar velocity dispersion in each galaxy. We adopt  $\sigma$  mainly from Prugniel and Simien (1996) and also from Faber et al. (1985) and Whitmore et al. (1985). For a given  $L_B\sigma^2$ , the X-ray extended galaxies show systematically larger  $L_X$  than the X-ray compact galaxies. The distribution against  $L_B\sigma^2$  is fitted in the same way, and the deviation  $s$  for the whole sample is 0.67. This is reduced to 0.37 by the exclusion of the X-ray extended galaxies. Some of the X-ray compact galaxies in clusters such as NGC 1404 and NGC 4365 show significant deviation from the linear relation. For the X-ray compact galaxies in clusters, the deviation  $s$  is 0.52. Thus, if we take only the X-ray compact field galaxies, it becomes 0.28. The best-fit slope for the  $L_X - L_B\sigma^2$  relation for the X-ray compact field galaxies is 1.3. No difference is seen between the X-ray compact elliptical and S0 galaxies; the average value of  $\log(L_X/L_B\sigma^2)$  for field elliptical and S0 galaxies are 24.85 (24.74-24.94) and 24.90 (24.70-25.05), respectively.

If stellar motion is the main heat source for the hot ISM, its X-ray luminosity should be approximated by the input rate of the kinetic energy of the gas from stellar mass loss. This is proportional to  $L_B\sigma^2$ , since mass loss rate is thought to be proportional to  $L_B$  (e.g. Ciotti et al. 1991). Figure 4 also shows expected energy input from the stellar mass loss, assuming a mass loss rate of  $1.5 \times 10^{-11}(L_B/L_\odot)M_\odot \text{ yr}^{-1}$  (Ciotti et al. 1991). The expected value looks like an upper envelope to the X-ray compact galaxies. The ISM luminosity of those with large  $L_B\sigma^2$  agrees well with this estimation, and fainter galaxies show slightly smaller values than the estimated level. Only 1 X-ray compact galaxy, NGC 1404 shows much higher luminosity than the relation. This galaxy is located near the center of the Fornax cluster, and therefore, interaction with the surrounding ICM may raise the ISM luminosity. These results support the view that the ISM in the X-ray compact galaxies is mainly heated by stellar motion. The input kinetic energy is probably balanced with the radiation loss in the X-ray emission, and a steady state is maintained.

### 3.3. ISM temperature

#### 3.3.1. Inner region

The obtained temperatures are mostly consistent with the previous results by various authors (Fabbiano et al. 1994, Pellegrini and Fabbiano, 1994, Trinchieri et al. 1997, Davis & White 1996, Irwin & Sarazin 1998b). Since Davis & White (1996) uses a 1 component spectral model, our values of the X-ray faintest galaxies are systematically lower, and consistent to those of the VSC (Kim et al. 1992; Fabbiano et al. 1994; Pellegrini et al. 1994; Irwin and Sarazin 1998a).

Figure 5 shows correlation between ISM temperature measured within  $4r_e$  and central stellar velocity dispersion,  $\sigma^2$ . In the correlation for the X-ray compact objects, the cluster objects show somewhat larger scatter than the field ones. The best-fit correlation for the the X-ray compact field elliptical galaxies is given by  $kT \propto \sigma^{1.8(+0.4,-0.4)}$  and shown with the solid line. Thus, the ISM temperature is proportional to the stellar velocity dispersion. The parameter  $\beta_{\text{spec}}$  denotes the ratio of stellar velocity dispersion to gas temperature, i.e.  $\beta_{\text{spec}} = \frac{\mu m_p \sigma^2}{kT}$  with  $\mu$  indicating a mean molecular weight in terms of the proton mass  $m_p$ . The plot shows that  $\beta_{\text{spec}}$  is about unity for these galaxies. Therefore, the ISM temperature in the X-ray compact galaxies is consistent with the kinetic energy of stellar motion.

The X-ray extended galaxies systematically exhibit a higher ISM temperature than the X-ray compact galaxies, indicating  $\beta_{\text{spec}}$  to be typically  $\sim 0.5$ . The correlation between  $\sigma^2$  and  $kT_s$  derived by Matsumoto et al. (1997), by Davis and White (1996) show a flatter slope, probably due to inclusion of both categories of galaxies in their samples.

### 3.3.2. ISM temperature profile

In order to look into a temperature structure, additional spectral fits are carried out for the data within  $1.5r_e$  and  $1.5\text{--}4r_e$ . An adjacent outer region is chosen for the background:  $1.5\text{--}3r_e$  and  $4\text{--}6r_e$ , respectively.

The problem in the spectral analysis is that the PSF for the PSPC is energy dependent (Boese 1999). For example, when the energy is 0.2 keV, only  $\sim 60\%$  of the photons from a point source at the on-axis is detected within  $0.5'$ . This fraction is more than 80% for an energy range 0.5–1.7 keV. The accumulation radius of such a small angular size would result in a wrong spectral feature in the sense that the inner region shows a harder spectrum. When the radius is raised to  $1'$ , the escaping photons to the outer annulus drop to 3% even at 0.2 keV. We therefore exclude objects which have  $1.5r_e < 1'$  for on-axis observations. The PSF also becomes broader in the outer regions of the PSPC field. When the source position is offset, we exclude it when the fraction of escaping photons from  $1.5r_e$  is larger than 5% at 0.2 keV. As a result, 14 galaxies are excluded. The fitting results are summarized in table 2.

Figure 6 compares the ISM temperatures in the central ( $r < 1.5r_e$ ) and outer ( $r > 1.5r_e$ ) regions. The X-ray extended galaxies all show positive temperature gradient with average values of  $kT(1.5 - 4r_e)/kT(< 1.5r_e)$ ,  $kT(4 - 12r_e)/kT(< 1.5r_e)$ , and  $kT(12 - 30r_e)/kT(< 1.5r_e)$  to be 1.28(1.27–1.29), 1.45(1.42–1.47) and 1.40(1.37–1.43), respectively. The X-ray compact galaxies show an average  $kT(1.5 - 4r_e)/kT(< 1.5r_e)$  to be 0.82–1.03, with fairly large uncertainty in each data set. Thus, even within  $4r_e$ , the temperature gradient is significantly different between the X-ray extended and the X-ray compact galaxies.

Figure 7 compares the ISM temperature against  $\sigma^2$  at the galaxy center. As shown in §3.3.1, values of  $\beta_{\text{spec}}$  for the X-ray compact galaxies are  $\sim 1.0$ . In contrast, The X-ray extended galaxies indicate  $\beta_{\text{spec}} = 0.5 - 1.0$  within  $1.5r_e$  and it drops to  $\sim 0.3 - 0.5$  in

$1.5r_e < r < 4r_e$ . Thus, at a given central  $\sigma$ , the temperature of the X-ray extended galaxies are systematically larger but the differences between the two categories are relatively small at the center.

## 4. Discussion

### 4.1. Origin of VSC

The PSPC spectra for the galaxies are well fitted with the two component model comprising a soft thin thermal emission with a temperature 0.1–1.0 keV and a hard bremsstrahlung component. The reported spectrum of VSC (e.g. Kim et al. 1992) has normalization and temperature consistent with our soft component.

If the VSC is due to stellar population, we expect their X-ray luminosity is proportional to the optical luminosity. In fact, the X-ray luminosity of the hard component show rather good correlation with  $L_B$  (Matsushita et al. 1994, Matsumoto et al. 1997, Matsushita et al. 2000). This result suggests that the hard component is mainly emitted from binary X-ray sources in the host galaxy, particularly low-mass X-ray binaries (LMXBs). However, even in the X-ray compact galaxies, there is still considerable scatter in the soft component luminosity against  $L_B$ .

As shown in §3.3, in the X-ray compact galaxies, the  $\beta_{\text{spec}}$  of the X-ray compact galaxies are about unity. Also their soft component luminosity shows a good correlation with a optical property,  $L_B\sigma^2$ . It is also established that the main source of the X-ray emission in luminous galaxies is the hot ISM (e.g. Forman et al. 1986, Trinchieri et al. 1987, Fabbiano 1989, Arimoto et al. 1997, Matsushita et al. 2000). These facts support the interpretation that the VSC comes from the ISM, which is confined by the gravitational potential. The VSC probably corresponds to the case that the soft component temperature

is very low,  $< 0.3$  keV.

## 4.2. ISM Mass

The ISM mass within  $4r_e$  is calculated by assuming the ISM brightness profile to be the same as the optical one. Within the optical radii, the measured X-ray profile, in fact, well agrees with the optical one for both X-ray extended galaxies, such as NGC 4636, NGC 4472, and NGC 1399 etc. (Forman et al. 1985, Trinchieri et al. 1994), and the X-ray compact galaxies including NGC 720 etc. (Buote et al. 1999). The obtained ISM masses within  $4r_e$  are plotted in figure 8. The X-ray compact galaxies indicate the mass to be  $10^{8\sim 9} M_\odot$ , which is about 0.1% of the stellar mass. The X-ray extended galaxies show  $10^{9\sim 10} M_\odot$ , about 1% of the stellar mass.

## 4.3. ISM luminosity of the X-ray compact galaxies; heating by stellar motion

When some galaxies in dense cluster environments are excluded, the ISM luminosity of the X-ray compact objects is consistent with the energy input from stellar mass loss (figure 4). The temperature of the ISM is consistent with the heating due to stellar motion, namely  $\beta_{\text{spec}} \sim 1$ . The ISM abundances derived from ASCA data are consistent with stellar metallicity (Matsushita et al. 2000). As a result, it is reasonable to conclude that the hot ISM in the X-ray compact galaxies is mainly supplied by the stellar mass loss.

The fact that several X-ray compact galaxies in clusters do not follow the general correlation suggests that interaction between ISM and surrounding ICM causes significant variation in the ISM luminosity.

The ISM in the X-ray compact galaxies is thought to be in a steady state, where input

energy is balanced with the radiative loss. The total ISM mass can be accumulated in only  $\sim 0.1$  Gyr by the stellar mass loss assuming the rate in Ciotti et al. (1991). This is the same order as the radiative cooling time scale (0.1 – 1 Gyr) and the dynamical time scale in galaxies ( $\sim 0.2$  Gyr). Therefore, the ISM in the X-ray compact galaxies reflects almost instantaneous balance between mass supply and outflow, as well as the balance between heating and cooling.

#### 4.4. External potential structure around the X-ray extended galaxies

Except a galaxy within a cluster, all of the galaxies with higher ISM luminosity than the stellar heating have largely extended X-ray emission with a radius of a few times of  $10r_e$ . Some other energy source is needed in addition to the kinematical heating due to the stellar motion. We found that luminosities within the optical radii and in the outer extended region correlate well. This suggests that the extended component, rather than the optical galaxy, has a strong influence on the ISM properties in the central region.

We have shown in Matsushita et al. (1998) that the X-ray extended galaxy, NGC 4636, is located at the bottom of an extended potential structure which is filled with a tenuous plasma. The present similarity in brightness profile and in temperature profile among the X-ray extended galaxies indicates that all these galaxies share essentially the same hierarchical potential structure. Temperature within  $1.5\text{--}4r_e$  in these galaxies is about twice as high as those in the X-ray compact galaxies, indicating that their potential is deeper than those in typical galaxies. We hence conclude that the X-ray extended galaxies are regarded as the central galaxy in a larger-scale potential structure corresponding, e.g., to galaxy groups.

There are a few galaxies with a smaller scale extended emission. However, their ISM

luminosity are consistent with the other X-ray compact galaxies. These galaxies may not be at the bottom of a potential, or increment of the X-ray luminosity due to such a smaller scale emission may be lower than the stellar heating.

Based on these results, Kodama & Matsushita (2000) compared optical properties and spatial extent of the X-ray emission. They found no significant difference in the stellar populations and suggested that the formation of stars predates the epoch when the dichotomy of the potential structure was established.

We note that, if one only looks at the central region, both the X-ray compact and the X-ray extended galaxies show a similar ISM temperature. Positive temperature gradients (low in the center) are usually interpreted in terms of cooling flows. However, the observed constancy in the ISM temperature suggests that the central cool temperature in the X-ray extended galaxies mainly reflects the galaxy potential, even though some part of the cool component may be produced by cooling flows.

## 5. Conclusion

The large scatter in the X-ray to optical luminosity ratio has been much reduced by the introduction of a single phenomenological parameter; whether the galaxy is “X-ray extended” or “X-ray compact”. Interaction between ISM and surrounding ICM also causes significant variation in the ISM luminosity.

The X-ray compact galaxies, excluding several galaxies in dense ICM environments, show tight correlation with kinematical energy input from stellar mass loss. Thus, the large scatter must have been caused by a sample mixture in the two categories.

I would like to thank Kazuo Makishima and Takaya Ohashi for valuable discussion.

This work was supported by the Japan Society for the Promotion of Science (JSPS) through its Postdoctoral Fellowship for Research Abroad and Research Fellowships for Young Scientists.

## REFERENCES

Anders, E., & Grevesse, N., 1989, *Geochim. Cosmochim. Acta*, 53,197

Anvi, Y., Soltan, A., Tananbaum, H., & Zamoraki, G, 1980, *ApJ*, 238, 800

Bender, R., Burstein, D., & Faber, S. M., 1993, *ApJ*, 411, 153

Beuing, J., Döbereiner, H., Böhringer, H., & Bender, R., 1999, *MNRAS*, 302, 209

Boese, F. G., 1999, *A&A*, 25,11

Buote, D. A. & Canizares, C. R. 1994, *ApJ*, 427, 86

Canizares, C.R., Fabbiano, G., & Trinchieri, G. 1987, *ApJ*, 312, 503

Ciotti, L., Pellegrini, S., Renzini, A., & D'Ercole, A. 1991, *ApJ*, 376, 380

Davis, D.S., & White, R.E., 1996, *ApJ*, 470, 35

de Vaucouleurs G., de Vaucouleurs A., Corwin Jr. H.G., Buta R.J., Paturel G., & Fouque P., 1991, *Third Reference Catalogue of Bright Galaxies (RC3 Catalog)*

Djorgovski, S. & Davis, M., 1987, *ApJ*, 313,59

Eskridge, P.B., Fabbiano, G., and Kim, D.-W., 1995, *ApJ*, 97, 141

Fabbiano, G., & Trinchieri, G., 1985, *ApJ*, 296, 430

Fabbiano, G., Kim, D.-W., & Trinchieri, G., 1992, *ApJS*, 80, 531

Fabbiano, G., Kim, D.-W., & Trinchieri, G., 1994, *ApJ*, 429, 94

Faber, S.M., Wegner, G., Burstein, D., Davies, R.L., Dressler, A., Lynden-Bell, D., Terlevich, R.J. 1989 *ApJS*, 69,763

Forman, W., Jones, C. & Tucker, W. 1985, ApJ, 293, 102

Ikebe, Y. et al. 1996, Nature, 379, 427

Irwin, J & Sarazin, C. L., 1998a, ApJ, 494, 33

Irwin, J & Sarazin, C. L., 1998b, ApJ, 499, 650

Kim, D.-W., Fabbiano, G., & Trinchieri, G. 1992, ApJ, 393, 134

Kodama, T., & Matsushita, K., 2000, accepted to ApJ

Mathews, W.G., & Fabrizio, B., 1998, ApJ, 493, 9

Matsumoto, H. et al. 1997, ApJ, 482, 133

Matsushita, K. et al. 1994, ApJ, 436, L41

Matsushita, K. 1997, Ph. D. Thesis, University of Tokyo

Matsushita, K., Makishima, K., Ikebe, Y., Rokutanda, E., Yamasaki, N., Y., & Ohashi, T. 1998, ApJ, 499, L13

Matsushita, K., Ohashi, T., & Makishima, K., 2000, PASJ, 52, 685

Pellegrini, S., & Fabbiano, G. 1994, ApJ, 429, 105

Prugniel, P., & Simien, F., 1996, A&A, 309, 749

Raymond, J.C., & Smith, B.W. 1977, ApJS, 35, 419

Trinchieri, G., & Fabbiano, G. 1985, ApJ, 296, 457

Trinchieri, G., Fabbiano, G. & Canizares, C. R. 1986, ApJ, 310, 673

Trinchieri, G., Kim, D.-W., Fabbiano, G. & Canizares, C. R. 1994, ApJ, 428, 555

Trinchieri, G., Fabbiano, G., & Kim, D.-W., 1997, A&A, 318, 361

Tully R. B. 1988, “*Nearby Galaxy Catalog*”, Cambridge University Press

White, R.E.III, & Sarazin, C.L. 1991, ApJ, 367, 476

Whitemore, B.C., McElroy, D. B., Tonry, J. L., 1985, ApJS, 50,1

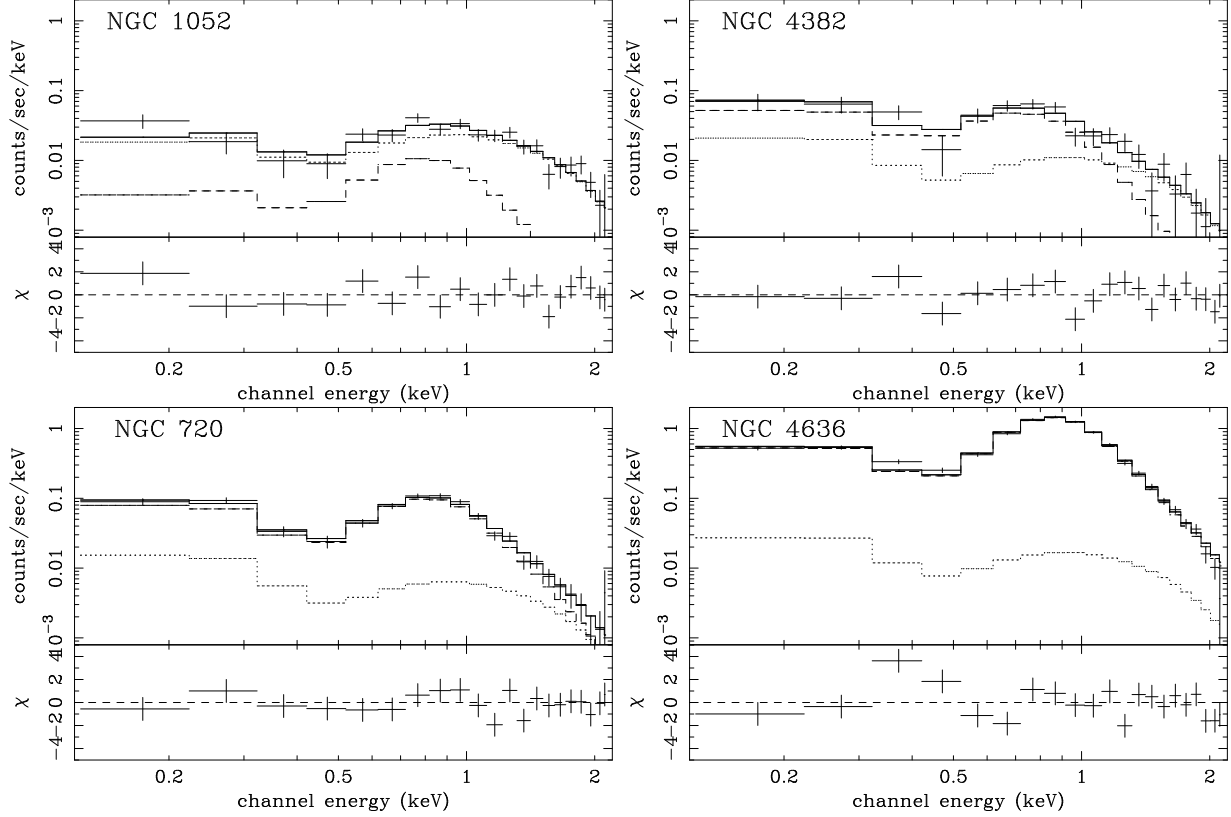


Fig. 1.— The PSPC spectra (crosses) of 4 representative galaxies fitted with the double-component model, consisting of a soft R-S component (dashed line) and a hard bremsstrahlung component (dotted line). The bottom panels show residuals of the fit.

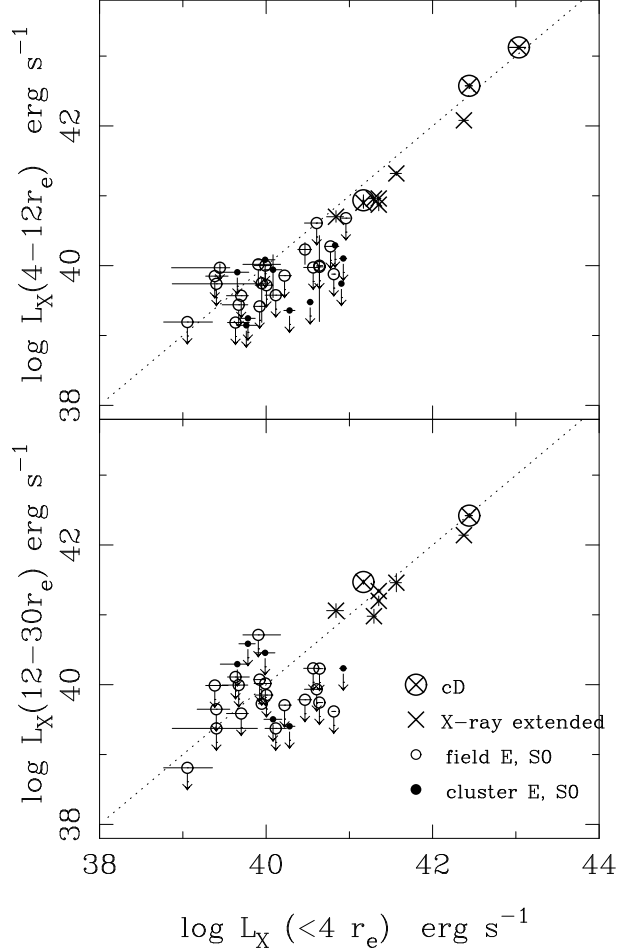


Fig. 2.— (upper panel)  $L_X(4-12r_e)$  and (lower panel)  $L_X(12-30r_e)$  of galaxies plotted against  $L_X(<4r_e)$ . Marks indicate galaxy categories for X-ray extended (crosses), cD galaxies (large open circles), field galaxies (open circles), and cluster galaxies (closed circles).

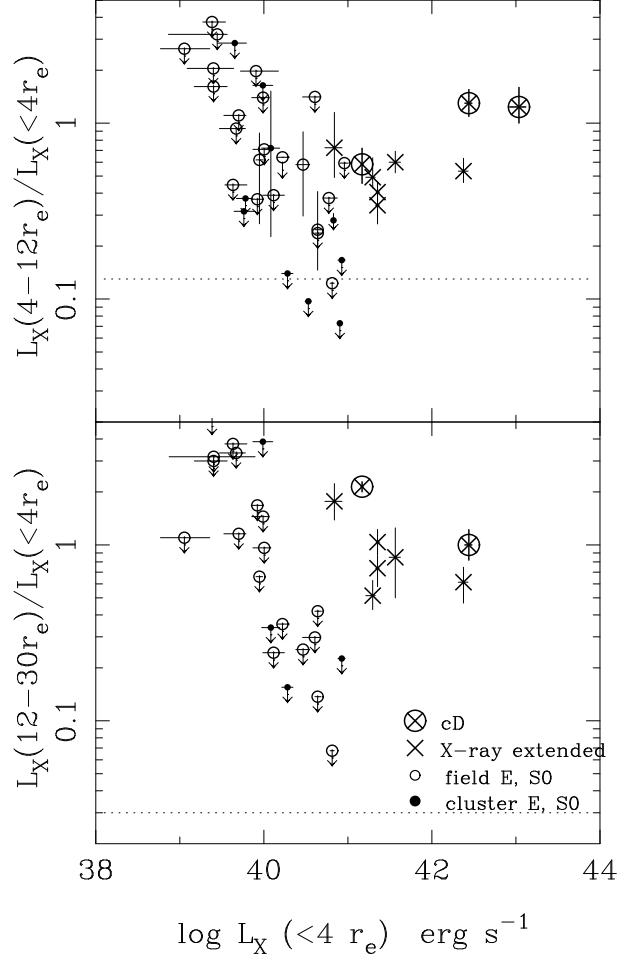


Fig. 3.— (upper panel) S4–12 ( $L_X(4-12r_e)/L_X(<4r_e)$ ) and (lower panel) S12–30 ( $L_X(12-30r_e)/L_X(<4r_e)$ ) are plotted against  $L_X(<4r_e)$ . Meanings of symbols are the same as figure 2. Dotted lines corresponds to ratio of optical profile.

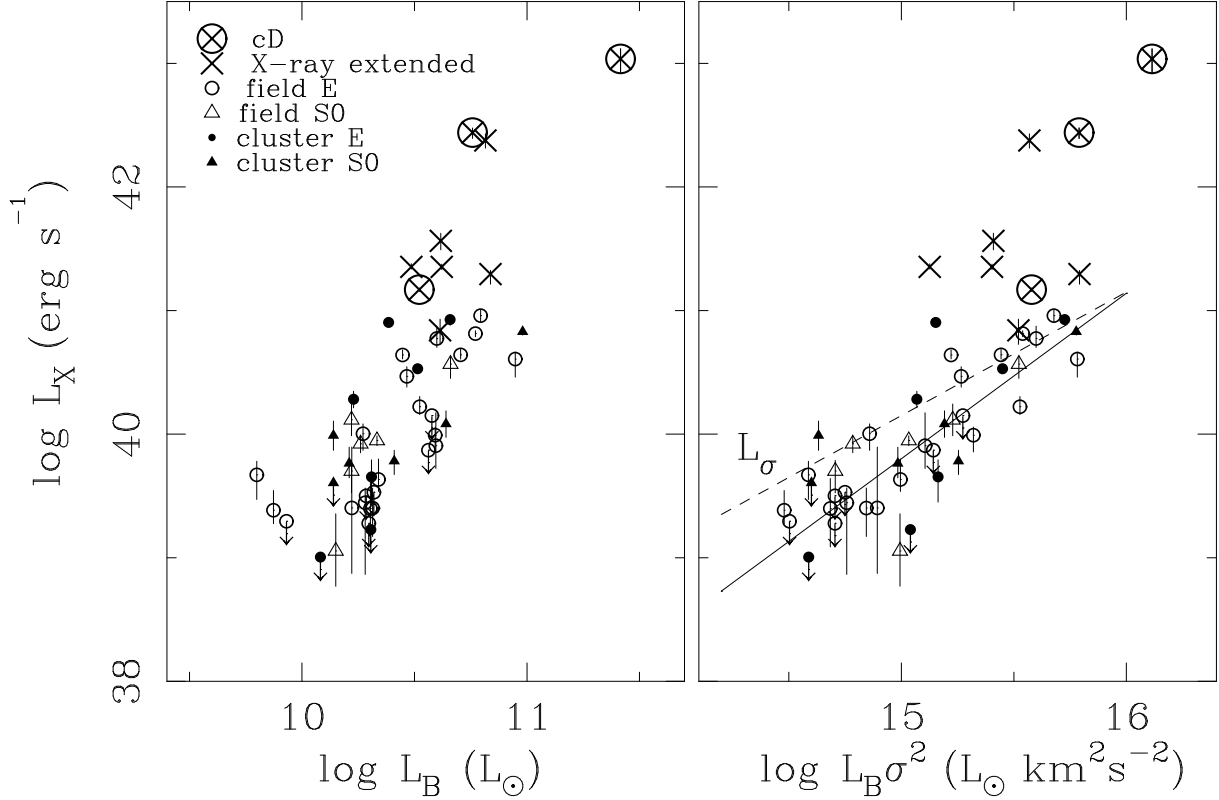


Fig. 4.—  $L_X(<4r_e)$  of galaxies plotted against  $L_B$  (left panel) and  $L_B \sigma^2$  (right panel). Marks indicate galaxy categories for X-ray extended (crosses), cD galaxies (large open circles), field ellipticals (open circles), field S0s (open triangles), cluster ellipticals (closed circles) and cluster S0s (closed triangles). The dashed line represents kinetic heating rate by stellar mass loss (see text in detail). The solid line corresponds to the best fit regression line among X-ray compact galaxies in the field.

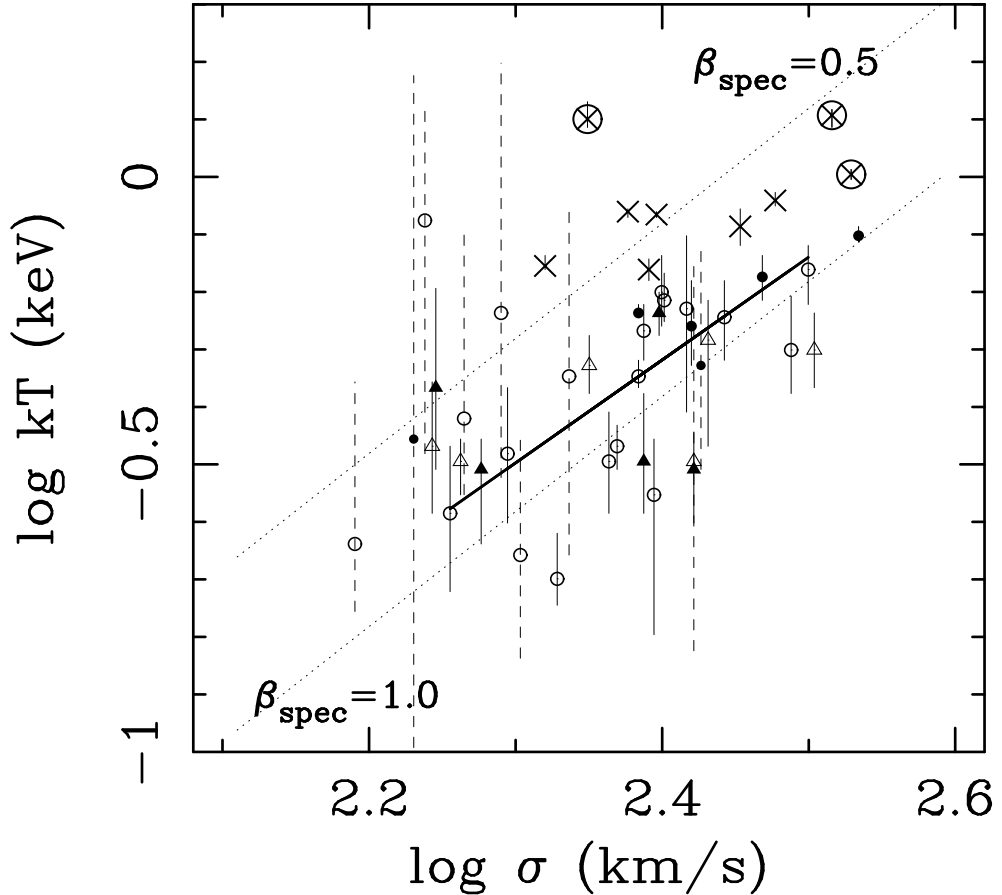


Fig. 5.— The ISM temperature within  $4 r_e$  vs.  $\sigma$ . Meanings of the symbols are the same as in figure 4. Solid line corresponds to best fit regression line for field elliptical galaxies. In order to emphasize the high quality data, the points with large error bars are represented in dashed lines. Dotted lines corresponds to  $\beta_{\text{spec}} = 0.5$  and 1.0.

$$CO = -4.612, LI = 1.789$$

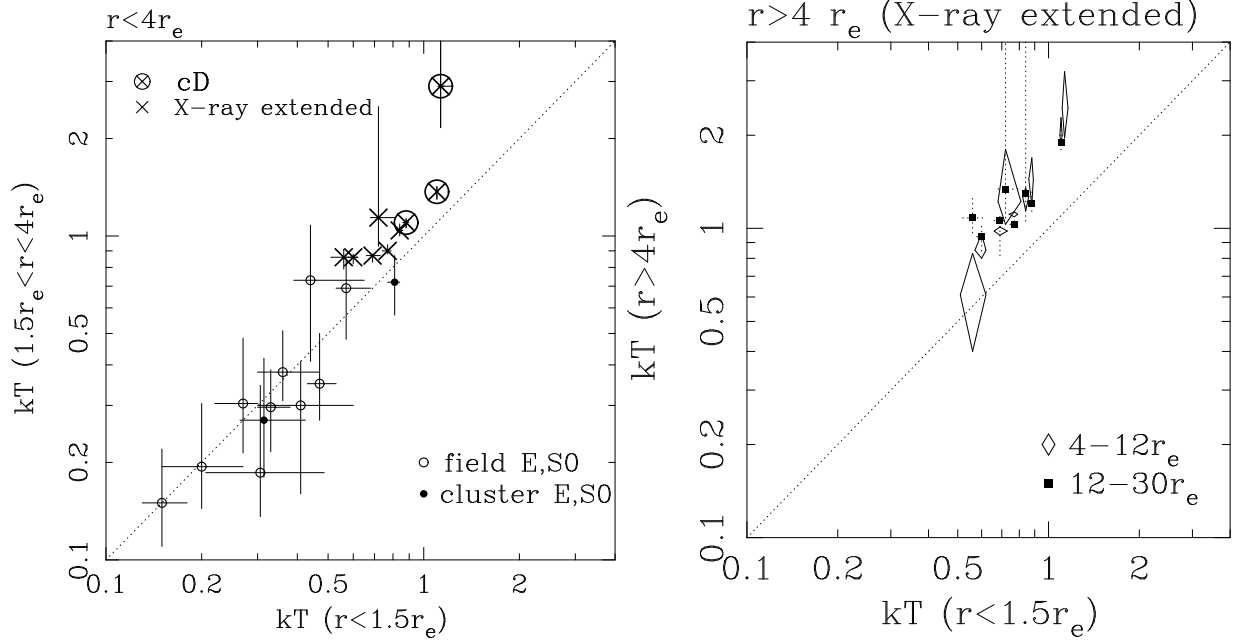


Fig. 6.— (a) ISM Temperatures within 1.5–4  $r_e$  vs. those in 1.5  $r_e$ . Meanings of the symbols are the same as in figure 2. Dotted line indicates the equal value for the two regions. (b) ISM temperatures in  $r > 4r_e$  vs. those in 1.5  $r_e$  of the X-ray extended galaxies. Marks indicate those in 4–12  $r_e$  (diamonds), and 12–30  $r_e$  (close squares), respectively.

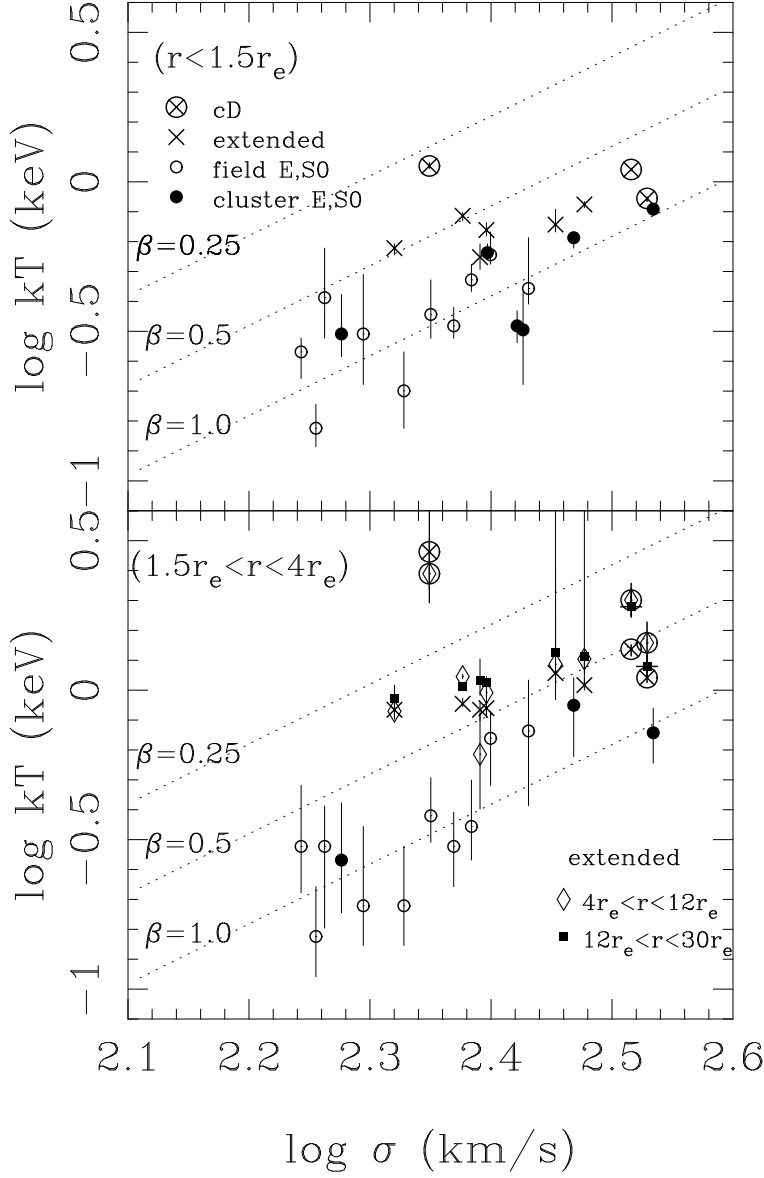


Fig. 7.— ISM temperature against  $\sigma$  within  $1.5 r_e$  (upper panel),  $1.5-4 r_e$  (lower panel). Marks indicate galaxy categories for X-ray extended (crosses), cD galaxies (large open circles), field galaxies (open circles), and cluster galaxies (closed circles). ISM temperature of the X-ray extended galaxies within  $4-12 r_e$  (diamonds) and  $12-30 r_e$  (closed squares) are also plotted.

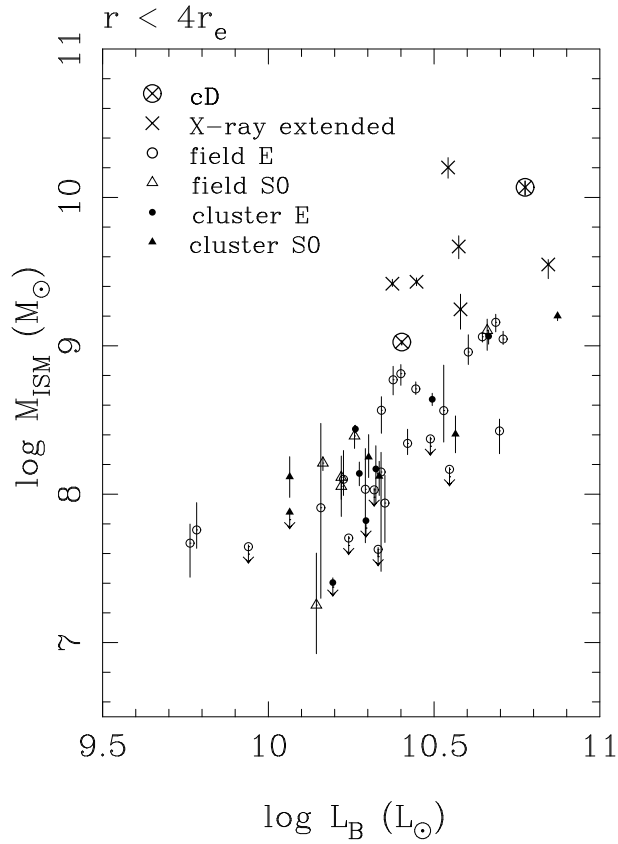


Fig. 8.— ISM mass within  $4 r_e$ . Meanings of the symbols are the same as in figure 4.

Table 1: The galaxy sample in the ROSAT archive data

galaxy	type <sup>a</sup>	$r_e^b$	exposure	offset <sup>c</sup>	note	galaxy	type <sup>a</sup>	$r_e^b$	exposure	offset <sup>c</sup>	note
		arcmin	s	arcmin				arcmin	s	arcmin	
NGC 524	-2.0	0.83	11171	13.7		NGC 4278	-5.0	0.58	3411	0.0	
NGC 596	-5.0	0.46	4055	12.6		NGC 4365	-5.0	0.83	14755	0.5	Virgo
NGC 720	-5.0	0.60	22819	0.2		NGC 4374	-5.0	0.85	22020	17.0	Virgo
NGC 1052	-5.0	0.56	13975	0.4		NGC 4382	-2.0	0.91	8495	0.5	Virgo
NGC 1316	-2.0	1.35	25173	0.2	Fornax	NGC 4406	-5.0	1.74	22020	0.3	Virgo
NGC 1332	-2.0	0.47	25307	7.1		NGC 4459	-2.0	0.59	7351	14.9	Virgo
NGC 1344	-5.0	0.45	4943	0.1		NGC 4472	-5.0	1.74	25951	0.2	Virgo
NGC 1380	-2.0	0.66	17766	0.8	Fornax	NGC 4473	-5.0	0.44	7351	20.8	Virgo
NGC 1395	-5.0	0.81	20464	0.3		NGC 4477	-2.0	0.63	7351	10.7	Virgo
NGC 1399	-5.0	0.68	53511	0.2	Fornax cD	NGC 4486	-5.0	1.58	30435	0.2	Virgo cD
NGC 1404	-5.0	0.40	53511	9.9	Fornax	NGC 4494	-5.0	0.81	12015	45.2	
NGC 1407	-5.0	1.17	22038	0.1		NGC 4526	-2.0	0.74	21354	0.2	Virgo
NGC 1549	-5.0	0.78	15300	2.9		NGC 4552	-5.0	0.49	16660	5.2	Virgo
NGC 1553	-2.0	1.10	15300	11.4		NGC 4621	-5.0	0.68	14148	25.1	Virgo
NGC 2768	-5.0	1.07	7664	0.1		NGC 4636	-5.0	1.48	13070	0.2	Virgo
NGC 3115	-2.0	0.54	7760	0.4		NGC 4649	-5.0	1.15	14148	1.0	Virgo
NGC 3193	-5.0	0.45	4617	7.7		NGC 4696	-4.0	3.53	14580	0.3	Cen cD
NGC 3557	-5.0	0.50	19616	0.1		NGC 4697	-5.0	1.20	9486	0.1	
NGC 3585	-5.0	0.60	5195	1.6		NGC 5044	-5.0	0.89	27730	0.2	
NGC 3607	-2.0	0.73	32757	0.2,7.7 <sup>d</sup>		NGC 5061	-5.0	0.44	6495	0.2	
NGC 3608	-5.0	0.56	32757	12.1,6.0 <sup>d</sup>		NGC 5322	-5.0	0.56	34778	0.2	
NGC 3610	-5.0	0.26	4606	0.2		NGC 5846	-5.0	1.05	8804	0.3	
NGC 3640	-5.0	0.54	15107	0.6		NGC 5866	-2.0	0.68	11993	0.5	
NGC 3923	-5.0	0.83	38818	0.1		NGC 6868	-5.0	0.56	11320	27.3	
NGC 4125	-5.0	0.98	10034	0.5		NGC 7144	-5.0	0.54	25851	0.3	
NGC 4261	-5.0	0.60	21893	0.3		IC 1459	-5.0	0.58	32694	0.3	

<sup>a</sup> Morphological type code by Tully (1988)

<sup>b</sup> Effective radius by RC3

<sup>c</sup> Offset angle from the detector center

<sup>d</sup> Two different pointings

Table 2: The results of spectral fitting procedure for annular regions. Errors show 90% confidence limits for a single parameter.

		Galactic	0–4 $r_e$	4–12 $r_e$	12–30 $r_e$	0–1.5 $r_e$	1.5–4 $r_e$
NGC 524	$kT^a$		$0.52^{+0.09}_{-0.18}$	0.52 (fix)	0.52 (fix)	$0.44^{+0.21}_{-0.05}$	$0.73^{+0.35}_{-0.32}$
	$N_H^b$	4.8	4.8 (fix)	4.8 (fix)	4.8 (fix)	4.8 (fix)	4.8 (fix)
	$F_{XISM}$		$3.0^{+0.5}_{-0.7} \times 10^{-13}$	$< 7.7 \times 10^{-14}$	$< 1.4 \times 10^{-13}$		
	$\chi^2/\nu$		19.6/18	11.8/16	41.3/30	13.8/17	19.0/18
NGC 596	$F_{XISM}$		$< 4.6 \times 10^{-14}$				
	$\chi^2/\nu$		16.0/16				
NGC 720	$kT$		$0.54^{+0.06}_{-0.06}$	0.54 (fix)	0.54 (fix)		
	$N_H$	1.7	$0.6^{+0.2}_{-0.2}$	1.7 (fix)	1.7 (fix)		
	$F_{XISM}$		$7.0^{+0.7}_{-0.5} \times 10^{-13}$	$1.7^{+0.9}_{-0.6} \times 10^{-13}$	$< 8.9 \times 10^{-14}$		
	$\chi^2/\nu$		14.8/16	24.3/33	21.1/20		
NGC 1052	$kT$		$0.45^{+0.42}_{-0.23}$	0.45 (fix)	0.45 (fix)		
	$N_H$	3.0	$2.1^{+1.1}_{-0.6}$	3.0 (fix)	3.0 (fix)		
	$F_{XISM}$		$6.1^{+12.9}_{-4.3} \times 10^{-14}$	$< 1.3 \times 10^{-13}$	$< 5.7 \times 10^{-14}$		
	$\chi^2/\nu$		21.4/16	10.6/18	51.5/35		
NGC 1316	$kT$		$0.58^{+0.05}_{-0.05}$	0.58 (fix)		$0.58^{+0.04}_{-0.03}$	$—^d$
	Fe <sup>c</sup>		$0.30^{+0.16}_{-0.10}$	0.50 (fix)		0.50 (fix)	0.50 (fix)
	$N_H$	1.7	$0.4^{+0.2}_{-0.1}$	1.7 (fix)		$0.8^{+0.2}_{-0.2}$	1.7 (fix)
	$F_{XISM}$		$1.6^{+0.1}_{-0.1} \times 10^{-12}$	$< 4.6 \times 10^{-13}$			
	$\chi^2/\nu$		21.1/15	29.5/31		22.8/17	32.6/35
NGC 1332	$kT$		$0.50^{+0.08}_{-0.07}$	0.50 (fix)	0.50 (fix)		
	$N_H$	2.1	$1.2^{+0.4}_{-0.4}$	2.1 (fix)	2.1 (fix)		
	$F_{XISM}$		$3.5^{+1.2}_{-0.9} \times 10^{-13}$	$< 1.0 \times 10^{-13}$	$< 6.3 \times 10^{-14}$		
	$\chi^2/\nu$		27.9/16	19.7/18	42.1/34		
NGC 1344	$F_{XISM}$		$< 4.5 \times 10^{-14}$				
	$\chi^2/\nu$		14.3/16				
NGC 1380	$kT$		$0.32^{+0.10}_{-0.06}$	0.32 (fix)			
	$N_H$	1.4	$0.4^{+0.4}_{-0.4}$	1.4 (fix)			
	$F_{XISM}$		$1.7^{+0.6}_{-0.4} \times 10^{-13}$	$< 4.1 \times 10^{-14}$			
	$\chi^2/\nu$		24.3/16	20.5/18			
NGC 1395	$kT$		$0.63^{+0.10}_{-0.08}$	$0.51^{+0.31}_{-0.20}$	0.63 (fix)	$0.57^{+0.11}_{-0.04}$	$0.69^{+0.16}_{-0.21}$
	$N_H$	1.8	$0.6^{+0.4}_{-0.2}$	1.8 (fix)	1.8 (fix)	$0.8^{+0.4}_{-0.3}$	$0.0^{+0.7}_{-0.0}$
	$F_{XISM}$		$5.5^{+1.1}_{-1.0} \times 10^{-13}$	$3.2^{+0.8}_{-1.2} \times 10^{-13}$	$< 1.1 \times 10^{-13}$		
	$\chi^2/\nu$		19.7/16	47.0/32	41.8/34	9.9/17	14.0/17
NGC 1399	$kT$		$1.01^{+0.02}_{-0.02}$	$1.44^{+0.25}_{-0.18}$	$1.20^{+0.11}_{-0.07}$	$0.88^{+0.01}_{-0.02}$	$1.10^{+0.03}_{-0.04}$
	Fe		$1.26^{+0.42}_{-0.16}$	$1.13^{+0.29}_{-0.15}$	$0.93^{+0.23}_{-0.15}$	$1.30^{+0.51}_{-0.30}$	$1.60^{+1.54}_{-0.40}$
	$N_H$	1.4	$1.2^{+0.2}_{-0.2}$	1.4 (fix)	1.4 (fix)	$1.3^{+0.2}_{-0.2}$	$0.7^{+0.5}_{-0.4}$
	$F_{XISM}$		$3.5^{+0.1}_{-0.1} \times 10^{-12}$	$2.0^{+0.4}_{-0.4} \times 10^{-12}$	$7.5^{+0.5}_{-0.5} \times 10^{-12}$		
	$\chi^2/\nu$		47.0/15	13.4/18	36.3/33	35.3/16	27.4/15

Table 2: (continued)

		Galactic	0–4 $r_e$	4–12 $r_e$	12–30 $r_e$	0–1.5 $r_e$	1.5–4 $r_e$
NGC 1404	$kT$		$0.58^{+0.02}_{-0.01}$	0.58 (fix)			
	Fe		$0.59^{+0.07}_{-0.06}$	0.50 (fix)			
	$N_H$	1.4	$1.0^{+0.1}_{-0.1}$	1.4 (fix)			
	$F_{X\text{ISM}}$		$1.9^{+0.1}_{-0.1} \times 10^{-12}$	$< 1.3 \times 10^{-13}$			
	$\chi^2/\nu$		77.5/15	41.8/30			
NGC 1407	$kT$		$0.82^{+0.06}_{-0.06}$	$1.22^{+0.58}_{-0.19}$	$1.34^{+11.7}_{-0.26}$	$0.72^{+0.09}_{-0.04}$	$1.14^{+1.37}_{-0.21}$
	$N_H$	5.2	$4.0^{+1.3}_{-0.9}$	5.2 (fix)	5.2 (fix)	$5.6^{+2.0}_{-1.0}$	5.2 (fix)
	$F_{X\text{ISM}}$		$1.3^{+0.3}_{-0.3} \times 10^{-12}$	$9.4^{+2.1}_{-1.6} \times 10^{-13}$	$2.3^{+0.6}_{-0.5} \times 10^{-12}$		
	$\chi^2/\nu$		18.8/16	31.2/30	39.9/35	13.7/17	12.3/18
NGC 1549	$kT$		$0.20^{+0.04}_{-0.02}$	0.20 (fix)	0.20 (fix)	$0.20^{+0.07}_{-0.05}$	$0.19^{+0.11}_{-0.05}$
	$N_H$	1.5	$0.0^{+1.0}_{-0.0}$	1.5 (fix)	1.5 (fix)	$0.1^{+1.2}_{-0.1}$	$0.0^{+0.7}_{-0.0}$
	$F_{X\text{ISM}}$		$1.5^{+0.7}_{-0.3} \times 10^{-13}$	$< 5.4 \times 10^{-14}$	$< 4.5 \times 10^{-13}$		
	$\chi^2/\nu$		26.6/16	13.4/16	29.9/35	28.7/17	22.5/16
NGC 1553	$kT$		$0.32^{+0.03}_{-0.04}$	0.32 (fix)	0.32 (fix)	$0.41^{+0.19}_{-0.11}$	$0.30^{+0.11}_{-0.14}$
	$N_H$	1.6	$0.0^{+0.8}_{-0.0}$	1.6 (fix)	1.6 (fix)	$0.0^{+0.2}_{-0.0}$	$0.0^{+0.2}_{-0.0}$
	$F_{X\text{ISM}}$		$3.9^{+0.6}_{-0.6} \times 10^{-13}$	$< 1.2 \times 10^{-13}$	$< 5.5 \times 10^{-13}$		
	$\chi^2/\nu$		26.6/16	16.7/20	19.6/27	21.9/14	24.4/17
NGC 2768	$kT$		$0.33^{+0.10}_{-0.08}$	0.33 (fix)	0.33 (fix)	$0.31^{+0.18}_{-0.10}$	$0.19^{+0.16}_{-0.05}$
	$N_H$	3.8	$1.8^{+2.3}_{-1.0}$	3.8 (fix)	3.8 (fix)	3.8 (fix)	3.8 (fix)
	$F_{X\text{ISM}}$		$3.0^{+0.6}_{-0.8} \times 10^{-13}$	$< 1.6 \times 10^{-13}$	$< 2.1 \times 10^{-13}$		
	$\chi^2/\nu$		15.3/16	30.1/33	39.6/33	11.8/18	8.1/16
NGC 3115	$kT$		$0.32^{+0.40}_{-0.17}$	0.32 (fix)	0.32 (fix)		
	$N_H$	4.5	4.5 (fix)	4.5 (fix)	4.5 (fix)		
	$F_{X\text{ISM}}$		$1.1^{+1.1}_{-0.5} \times 10^{-13}$	$< 1.5 \times 10^{-13}$	$< 6.3 \times 10^{-14}$		
	$\chi^2/\nu$		23.6/16	17.5/20	34.6/35		
NGC 3193	$F_{X\text{ISM}}$		$< 5.7 \times 10^{-14}$				
	$\chi^2/\nu$		23.0/16				
NGC 3557	$kT$		$0.59^{+0.20}_{-0.20}$	0.59 (fix)	0.59 (fix)		
	$N_H$	8.3	8.3 (fix)	8.3 (fix)	8.3 (fix)		
	$F_{X\text{ISM}}$		$2.1^{+0.3}_{-0.6} \times 10^{-13}$	$< 2.1 \times 10^{-13}$	$< 4.5 \times 10^{-14}$		
	$\chi^2/\nu$		11.0/16	55.9/31	70.0/30		
NGC 3585	$F_{X\text{ISM}}$		$< 3.0 \times 10^{-13}$				
	$\chi^2/\nu$		16.0/16				
NGC 3607	$kT$		$0.47^{+0.06}_{-0.05}$	0.47 (fix)	0.47 (fix)	$0.36^{+0.11}_{-0.06}$	$0.38^{+0.13}_{-0.07}$
	$N_H$	1.4	$0.1^{+0.2}_{-0.1}$	1.4 (fix)	1.4 (fix)	$0.0^{+0.4}_{-0.0}$	$0.3^{+1.1}_{-0.3}$
	$F_{X\text{ISM}}$		$3.3^{+0.3}_{-0.3} \times 10^{-13}$	$2.2^{+0.5}_{-1.3} \times 10^{-13}$	$< 2.0 \times 10^{-13}$		
	$\chi^2/\nu$		14.9/16	35.1/33	50.0/34	18.2/17	24.9/17

Table 2: (continued)

		Galactic	0–4 $r_e$	4–12 $r_e$	12–30 $r_e$	0–1.5 $r_e$	1.5–4 $r_e$
NGC 3608	$kT$		$0.22^{+0.13}_{-0.08}$	0.22 (fix)	0.22 (fix)		
	$N_H$	1.4	$0.5^{+1.1}_{-0.5}$	1.4 (fix)	1.4 (fix)		
	$F_{\text{XISM}}$		$9.0^{+4.0}_{-2.0} \times 10^{-14}$	$< 2.6 \times 10^{-13}$	$< 3.9 \times 10^{-13}$		
	$\chi^2/\nu$		13.3/16	13.4/19	50.0/34		
NGC 3610	$F_{\text{XISM}}$		$< 4.4 \times 10^{-14}$				
	$\chi^2/\nu$		9.4/16				
NGC 3640	$kT$		$0.38^{+0.42}_{-0.11}$	0.38 (fix)	0.38 (fix)		
	$N_H$	6.7	6.7 (fix)	6.7 (fix)	6.7 (fix)		
	$F_{\text{XISM}}$		$5.1^{+2.3}_{-2.1} \times 10^{-14}$	$< 4.9 \times 10^{-14}$	$< 9.0 \times 10^{-14}$		
	$\chi^2/\nu$		13.5/17	16.5/17	13.0/16		
NGC 3923	$kT$		$0.45^{+0.03}_{-0.02}$	0.45 (fix)	0.45 (fix)	$0.47^{+0.06}_{-0.04}$	$0.35^{+0.15}_{-0.08}$
	$N_H$	6.0	6.0 (fix)	6.0 (fix)	6.0 (fix)	$5.2^{+2.3}_{-1.2}$	6.0 (fix)
	$F_{\text{XISM}}$		$8.9^{+0.5}_{-0.5} \times 10^{-13}$	$< 1.0 \times 10^{-13}$	$< 5.7 \times 10^{-14}$		
	$\chi^2/\nu$		13.2/16	8.5/19	30.5/30	22.1/17	8.4/18
NGC 4125	$kT$		$0.34^{+0.03}_{-0.03}$	0.34 (fix)	0.34 (fix)	$0.33^{+0.05}_{-0.03}$	$0.30^{+0.09}_{-0.08}$
	$N_H$	1.8	$0.4^{+0.4}_{-0.3}$	1.8 (fix)	1.8 (fix)	$0.7^{+0.4}_{-0.4}$	$0.1^{+0.9}_{-0.1}$
	$F_{\text{XISM}}$		$6.6^{+0.7}_{-0.5} \times 10^{-13}$	$< 1.4 \times 10^{-13}$	$< 2.6 \times 10^{-13}$		
	$\chi^2/\nu$		27.2/16	34.8/33	41.3/33	40.0/35	29.8/35
NGC 4261	$kT$		$0.69^{+0.07}_{-0.09}$	0.69 (fix)			
	$N_H$	1.5	$1.0^{+0.2}_{-0.3}$	1.5 (fix)			
	$F_{\text{XISM}}$		$5.8^{+1.5}_{-0.9} \times 10^{-13}$	$< 1.8 \times 10^{-13}$			
	$\chi^2/\nu$		12.4/16	46.2/33			
NGC 4278	$kT$		$0.28^{+0.07}_{-0.12}$	0.28 (fix)	0.28 (fix)		
	$N_H$	1.7	$0.0^{+1.8}_{-0.0}$	1.7 (fix)	1.7 (fix)		
	$F_{\text{XISM}}$		$3.8^{+1.1}_{-1.4} \times 10^{-13}$	$< 2.2 \times 10^{-13}$	$< 8.0 \times 10^{-13}$		
	$\chi^2/\nu$		7.1/16	10.9/16	20.5/16		
NGC 4365	$kT$		$0.47^{+0.29}_{-0.16}$	0.47 (fix)	0.47 (fix)	$0.32^{+0.11}_{-0.11}$	— <sup>d</sup>
	$N_H$	1.6	$0.5^{+0.5}_{-0.4}$	1.6 (fix)	1.6 (fix)	$1.4^{+1.2}_{-0.7}$	1.6 (fix)
	$F_{\text{XISM}}$		$1.6^{+0.6}_{-0.6} \times 10^{-13}$	$< 2.9 \times 10^{-13}$	$< 7.0 \times 10^{-13}$		
	$\chi^2/\nu$		11.0/16	16.1/18		24.3/17	9.2/17
NGC 4374	$kT$		$0.67^{+0.06}_{-0.06}$	0.67 (fix)			
	$N_H$	2.6	$1.2^{+0.2}_{-0.2}$	2.6 (fix)			
	$F_{\text{XISM}}$		$1.2^{+0.1}_{-0.1} \times 10^{-12}$	$< 1.1 \times 10^{-13}$			
	$\chi^2/\nu$		19.1/16	46.2/33			
NGC 4382	$kT$		$0.31^{+0.04}_{-0.08}$	0.31 (fix)	0.31 (fix)	$0.31^{+0.11}_{-0.05}$	$0.27^{+0.15}_{-0.09}$
	$N_H$	2.5	$0.8^{+0.7}_{-0.5}$	2.5 (fix)	2.5 (fix)	$1.8^{+1.4}_{-0.9}$	$1.0^{+1.1}_{-1.0}$
	$F_{\text{XISM}}$		$3.6^{+1.0}_{-0.8} \times 10^{-13}$	$2.6^{+1.7}_{-1.6} \times 10^{-13}$	$< 9.5 \times 10^{-14}$		
	$\chi^2/\nu$		20.4/16	28.2/32	50.3/37	9.9/17	18.1/17

Table 2: (continued)

		Galactic	0–4 $r_e$	4–12 $r_e$	12–30 $r_e$	0–1.5 $r_e$	1.5–4 $r_e$
NGC 4406	$kT$		$0.86^{+0.01}_{-0.01}$	$1.00^{+0.01}_{-0.05}$	$1.06^{+0.06}_{-0.25}$	$0.69^{+0.04}_{-0.03}$	$0.87^{+0.01}_{-0.04}$
	Fe		$0.90^{+0.31}_{-0.06}$	$1.0 > 0.8$	$0.30^{+0.63}_{-0.20}$	$0.68^{+0.15}_{-0.14}$	$1.20 > 1.0$
	$N_H$	2.6	$1.7^{+0.1}_{-0.2}$	2.6 (fix)	2.6 (fix)	$1.4^{+0.4}_{-0.4}$	$1.5^{+0.4}_{-0.5}$
	$F_{X\text{ISM}}$		$1.3^{+0.1}_{-0.1} \times 10^{-11}$	$7.8^{+0.5}_{-0.5} \times 10^{-12}$	$1.1^{+0.4}_{-0.4} \times 10^{-11}$		
	$\chi^2/\nu$		28.1/16	26.1/16	36.5/33	17.8/16	20.1/16
NGC 4459	$F_{X\text{ISM}}$		$< 1.2 \times 10^{-13}$				
	$\chi^2/\nu$		13.4/16				
NGC 4472	$kT$		$0.91^{+0.03}_{-0.02}$	$1.27^{+0.08}_{-0.13}$	$1.30^{+4.10}_{-0.25}$	$0.84^{+0.02}_{-0.02}$	$1.04^{+0.05}_{-0.04}$
	Fe		$1.52^{+1.20}_{-0.24}$	$1.13^{+1.35}_{-0.53}$	1.13 (fix)	$1.5^{+1.3}_{-0.4}$	$1.8 > 1.4$
	$N_H$	1.7	$1.0^{+0.1}_{-0.1}$	1.7 (fix)	1.7 (fix)	$1.1^{+0.2}_{-0.2}$	$1.1^{+0.4}_{-0.3}$
	$F_{X\text{ISM}}$		$7.0^{+0.5}_{-1.2} \times 10^{-12}$	$3.4^{+0.4}_{-0.4} \times 10^{-12}$	$3.6^{+0.8}_{-0.6} \times 10^{-12}$		
	$\chi^2/\nu$		19.8/16	32.3/36	31.7/35	19.4/16	16.4/16
NGC 4473	$F_{X\text{ISM}}$		$< 3.6 \times 10^{-14}$				
	$\chi^2/\nu$		9.2/17				
NGC 4477	$kT$		$0.43^{+0.21}_{-0.12}$	0.43 (fix)	0.43 (fix)		
	$N_H$	2.6	$0.0^{+0.6}_{-0.0}$	2.6 (fix)	2.6 (fix)		
	$F_{X\text{ISM}}$		$2.9^{+0.9}_{-0.7} \times 10^{-13}$	$< 3.6 \times 10^{-13}$	$< 8.5 \times 10^{-13}$		
	$\chi^2/\nu$		13.6/16	21.5/33	25.6/23		
NGC 4486	$kT$		$1.28^{+0.03}_{-0.06}$	$2.00^{+0.28}_{-0.12}$	$1.90^{+0.29}_{-0.13}$	$1.10^{+0.01}_{-0.01}$	$1.37^{+0.05}_{-0.07}$
	Fe		$0.94^{+0.05}_{-0.08}$	0.94 (fix)	0.94 (fix)	$0.97^{+0.06}_{-0.06}$	$1.0^{+0.16}_{-0.13}$
	$N_H$	2.6	$1.5^{+0.1}_{-0.1}$	2.6 (fix)	2.6 (fix)	$1.3^{+0.1}_{-0.1}$	$1.3^{+0.1}_{-0.1}$
	$F_{X\text{ISM}}$		$1.0^{+0.1}_{-0.1} \times 10^{-10}$	$1.3^{+0.1}_{-0.1} \times 10^{-10}$	$1.0^{+0.1}_{-0.1} \times 10^{-10}$		
	$\chi^2/\nu$		65.9/17	40.7/21	86.5/26	59.5/16	20.3/16
NGC 4494	$kT$		$0.23^{+0.21}_{-0.06}$	0.23 (fix)			
	$N_H$	1.5	1.5 (fix)	1.5 (fix)			
	$F_{X\text{ISM}}$		$8.6^{+6.4}_{-4.4} \times 10^{-14}$	$< 1.6 \times 10^{-13}$			
	$\chi^2/\nu$		13.5/17	15.5/17			
NGC 4526	$kT$		$0.31^{+0.05}_{-0.06}$	0.31 (fix)	0.31 (fix)	$0.33^{+0.04}_{-0.04}$	— <sup>d</sup>
	$N_H$	1.6	$0.0^{+1.0}_{-0.0}$	1.6 (fix)	1.6 (fix)	1.6 (fix)	1.6 (fix)
	$F_{X\text{ISM}}$		$1.8^{+0.4}_{-0.4} \times 10^{-13}$	$< 5.2 \times 10^{-14}$	$< 1.2 \times 10^{-13}$		
	$\chi^2/\nu$		27.7/16	38.4/35	28.4/24	32.7/17	19.1/18
NGC 4552	$kT$		$0.55^{+0.11}_{-0.08}$	0.55 (fix)	0.55 (fix)		
	$N_H$	2.6	$1.7^{+0.4}_{-0.3}$	2.6 (fix)	2.6 (fix)		
	$F_{X\text{ISM}}$		$6.8^{+1.1}_{-1.0} \times 10^{-13}$	$< 8.1 \times 10^{-14}$	$< 9.0 \times 10^{-14}$		
	$\chi^2/\nu$		23.3/16	22.2/33	27.4/27		
NGC 4621	$F_{X\text{ISM}}$		$< 6.0 \times 10^{-14}$				
	$\chi^2/\nu$		14.4/17				

Table 2: (continued)

		Galactic	0–4 $r_e$	4–12 $r_e$	12–30 $r_e$	0–1.5 $r_e$	1.5–4 $r_e$
NGC 4636	$kT$		$0.70^{+0.03}_{-0.01}$	$0.85^{+0.11}_{-0.05}$	$0.94^{+0.10}_{-0.10}$	$0.60^{+0.02}_{-0.03}$	$0.86^{+0.02}_{-0.04}$
	Fe		$0.82^{+0.11}_{-0.08}$	$0.50^{+0.15}_{-0.24}$	$0.86^{+1.16}_{-0.45}$	$0.70^{+0.22}_{-0.10}$	$2.0 > 1.1$
	$N_H$	1.8	$1.6^{+0.1}_{-0.1}$	1.8 (fix)	1.8 (fix)	$1.4^{+0.2}_{-0.1}$	$0.8^{+0.7}_{-0.4}$
	$F_{X\text{ISM}}$		$8.0^{+0.5}_{-0.3} \times 10^{-12}$	$3.2^{+0.3}_{-0.2} \times 10^{-12}$	$8.3^{+1.5}_{-1.3} \times 10^{-12}$		
	$\chi^2/\nu$		35.1/16	37.5/33	65.6/50	28.3/16	12.7/16
NGC 4649	$kT$		$0.79^{+0.03}_{-0.02}$	0.79 (fix)	0.79 (fix)	$0.81^{+0.03}_{-0.04}$	$0.72^{+0.15}_{-0.15}$
	Fe		$1.30^{+3.20}_{-0.70}$	0.50 (fix)	0.50 (fix)	$1.60 > 1.0$	0.50 (fix)
	$N_H$	2.0	$2.4^{+0.3}_{-0.3}$	2.0 (fix)	2.0 (fix)	$1.6^{+0.5}_{-0.7}$	$1.7^{+2.0}_{-0.8}$
	$F_{X\text{ISM}}$		$3.0^{+0.3}_{-0.3} \times 10^{-12}$	$< 4.5 \times 10^{-13}$	$< 6.1 \times 10^{-13}$		
	$\chi^2/\nu$		25.5/16	38.0/33		10.2/15	13.9/17
NGC 4696	$kT$		$1.26^{+0.09}_{-0.04}$	$2.45^{+0.76}_{-0.49}$		$1.13^{+0.03}_{-0.02}$	$2.90^{+1.60}_{-0.74}$
	Fe		$0.97^{+0.32}_{-0.14}$	1.0 (fix)		$0.84^{+0.29}_{-0.22}$	1.0 (fix)
	$N_H$	8.1	$6.9^{+0.5}_{-0.4}$	8.1 (fix)		$9.4^{+1.2}_{-0.8}$	8.1 (fix)
	$F_{X\text{ISM}}$		$5.5^{+0.9}_{-1.0} \times 10^{-11}$	$6.8^{+0.4}_{-0.4} \times 10^{-11}$			
	$\chi^2/\nu$		73.0/59	17.0/17		21.5/16	36.5/33
NGC 4697	$kT$		$0.26^{+0.08}_{-0.07}$	0.26 (fix)	0.26 (fix)	$0.15^{+0.03}_{-0.02}$	$0.15^{+0.07}_{-0.04}$
	$N_H$	2.1	$0.2^{+0.8}_{-0.2}$	2.1 (fix)	2.1 (fix)	2.1 (fix)	2.1 (fix)
	$F_{X\text{ISM}}$		$2.6^{+2.2}_{-0.9} \times 10^{-13}$	$< 3.4 \times 10^{-13}$	$< 1.7 \times 10^{-12}$		
	$\chi^2/\nu$		30.0/16	41.6/33	44.7/35	15.7/17	28.6/15
NGC 5044	$kT$		$0.87^{+0.01}_{-0.02}$	$1.11^{+0.02}_{-0.02}$	$1.03^{+0.03}_{-0.03}$	$0.77^{+0.02}_{-0.03}$	$0.90^{+0.04}_{-0.02}$
	Fe		$1.60^{+0.50}_{-0.30}$	$1.57^{+0.15}_{-0.13}$	$0.64^{+0.15}_{-0.12}$	$1.38^{+0.51}_{-0.40}$	$2.44^{+1.80}_{-0.50}$
	$N_H$	4.9	$3.7^{+0.2}_{-0.2}$	4.9 (fix)	4.9 (fix)	$3.6^{+0.3}_{-0.3}$	$3.5^{+0.4}_{-0.5}$
	$F_{X\text{ISM}}$		$1.5^{+0.2}_{-0.2} \times 10^{-11}$	$8.0^{+0.2}_{-0.2} \times 10^{-12}$	$9.2^{+2.0}_{-2.2} \times 10^{-12}$		
	$\chi^2/\nu$		28.9/16	19.4/17	49.0/30	14.6/15	24.5/15
NGC 5061	$F_{X\text{ISM}}$		$< 1.0 \times 10^{-13}$				
	$\chi^2/\nu$		21.2/17				
NGC 5322	$kT$		$0.32^{+0.07}_{-0.06}$	0.32 (fix)	0.32 (fix)		
	$N_H$	1.6	$0.0^{+1.0}_{-0.0}$	1.6 (fix)	1.6 (fix)		
	$F_{X\text{ISM}}$		$1.2^{+0.2}_{-0.3} \times 10^{-13}$	$< 1.2 \times 10^{-13}$	$< 1.3 \times 10^{-13}$		
	$\chi^2/\nu$		29.3/16	17.6/19	35.0/30		
NGC 5846	$kT$		$0.69^{+0.03}_{-0.03}$	$0.61^{+0.22}_{-0.21}$	$1.08^{+0.19}_{-0.12}$	$0.56^{+0.06}_{-0.05}$	$0.86^{+0.05}_{-0.07}$
	Fe		$1.06^{+5.54}_{-0.42}$	$1.0 > 0.40$	$0.64 > 0.14$	$1.2^{+1.1}_{-0.5}$	$1.6 > 0.6$
	$N_H$	4.2	$2.8^{+0.6}_{-0.5}$	4.2 (fix)	4.2 (fix)	$2.9^{+0.9}_{-1.0}$	$2.6^{+1.1}_{-0.7}$
	$F_{X\text{ISM}}$		$3.8^{+0.2}_{-0.2} \times 10^{-12}$	$1.3^{+0.2}_{-0.2} \times 10^{-12}$	$2.8^{+0.5}_{-0.6} \times 10^{-12}$		
	$\chi^2/\nu$		14.0/16	46.5/33	32.2/25	18.2/15	21.8/17

Table 2: (continued)

		Galactic	0–4 $r_e$	4–12 $r_e$	12–30 $r_e$	0–1.5 $r_e$	1.5–4 $r_e$
NGC 5866	$kT$		$0.34^{+0.10}_{-0.08}$	0.34 (fix)	0.34 (fix)	$0.27^{+0.03}_{-0.05}$	$0.30^{+0.18}_{-0.09}$
	$N_H$	1.5	$0.0^{+0.5}_{-0.0}$	1.5 (fix)	1.5 (fix)	$0.0^{+2.7}_{-0.0}$	$0.0^{+1.5}_{-0.0}$
	$F_{X\text{ISM}}$		$1.8^{+0.4}_{-0.6} \times 10^{-13}$	$< 1.3 \times 10^{-13}$	$< 1.4 \times 10^{-13}$		
	$\chi^2/\nu$		12.9/16	26.8/33	62.7/39	23.8/16	20.0/16
NGC 6868	$kT$		$0.57^{+0.09}_{-0.09}$	0.57 (fix)			
	$N_H$	4.9	4.9 (fix)	4.9 (fix)			
	$F_{X\text{ISM}}$		$5.2^{+0.6}_{-0.6} \times 10^{-13}$	$< 2.7 \times 10^{-13}$			
	$\chi^2/\nu$		28.6/17	14.9/17			
NGC 7144	$kT$		$0.84^{+0.47}_{-0.51}$	0.84 (fix)	0.84 (fix)		
	$N_H$	2.9	$0.4^{+4.2}_{-0.4}$	2.9 (fix)	2.9 (fix)		
	$F_{X\text{ISM}}$		$3.8^{+1.2}_{-2.8} \times 10^{-14}$	$< 3.2 \times 10^{-14}$	$< 5.0 \times 10^{-13}$		
	$\chi^2/\nu$		15.5/16	17.4/16	41.8/35		
IC 1459	$kT$		$0.50^{+0.12}_{-0.08}$	0.50 (fix)	0.50 (fix)		
	$N_H$	1.2	$0.6^{+0.2}_{-0.2}$	1.2 (fix)	1.2 (fix)		
	$F_{X\text{ISM}}$		$2.9^{+0.6}_{-0.4} \times 10^{-13}$	$< 1.6 \times 10^{-13}$	$< 8.9 \times 10^{-14}$		
	$\chi^2/\nu$		10.4/16	24.9/13	18.5/15		

a: (keV)

b: ( $10^{20}\text{cm}^{-2}$ )

c: (solar)

d: not constrained

Table 3: Fit to the distribution function. Errors show 90% confidence limits

sample	X	a	b	s
whole	$\log(L_B) - 11$	1.9 (1.7–2.1)	41.3	0.70 (0.60–0.80)
X-ray extended	$\log(L_B) - 11$	1.8 (1.2–2.4)	42.5	0.40 (0.30–0.62)
compact	$\log(L_B) - 11$	1.5 (1.3–1.7)	40.8	0.45 (0.40–0.50)
whole	$\log(L_B\sigma^2) - 16.0$	1.35 (1.30–1.40)	41.4	0.67 (0.58–0.74)
X-ray extended	$\log(L_B\sigma^2) - 16.0$	1.6 (0.5–2.5)	42.3	0.52 (0.39–0.76)
compact	$\log(L_B\sigma^2) - 16.0$	1.40 (1.20–1.60)	41.1	0.38 (0.32–0.46)
field compact	$\log(L_B\sigma^2) - 16.0$	1.34 (1.08–1.60)	41.1	0.28 (0.22–0.38)
cluster compact	$\log(L_B\sigma^2) - 16.0$	1.3 (0.9–1.5)	41.1	0.52 (0.40–0.78)

Fits are of the form  $\log L_X = aX + b$ , with the standard deviation  $s$ .